



UNIVERSITY OF LEEDS

This is a repository copy of *Memory-Assisted Quantum Key Distribution with a Single Nitrogen-Vacancy Center*.

White Rose Research Online URL for this paper:
<http://eprints.whiterose.ac.uk/120756/>

Version: Accepted Version

Article:

Lo Piparo, N, Razavi, M orcid.org/0000-0003-4172-2125 and Munro, WJ (2017)
Memory-Assisted Quantum Key Distribution with a Single Nitrogen-Vacancy Center.
Physical Review A, 96 (5). 052313. ISSN 2469-9926

<https://doi.org/10.1103/PhysRevA.96.052313>

© 2017 American Physical Society. This is an author produced version of a paper published in Physical Review A. Uploaded in accordance with the publisher's self-archiving policy.

Reuse

Unless indicated otherwise, fulltext items are protected by copyright with all rights reserved. The copyright exception in section 29 of the Copyright, Designs and Patents Act 1988 allows the making of a single copy solely for the purpose of non-commercial research or private study within the limits of fair dealing. The publisher or other rights-holder may allow further reproduction and re-use of this version - refer to the White Rose Research Online record for this item. Where records identify the publisher as the copyright holder, users can verify any specific terms of use on the publisher's website.

Takedown

If you consider content in White Rose Research Online to be in breach of UK law, please notify us by emailing eprints@whiterose.ac.uk including the URL of the record and the reason for the withdrawal request.



eprints@whiterose.ac.uk
<https://eprints.whiterose.ac.uk/>

Memory-Assisted Quantum Key Distribution with a Single Nitrogen Vacancy Center

Nicoló Lo Piparo,^{1,2} Mohsen Razavi,¹ and William J. Munro^{2,3}

¹*School of Electronic and Electrical Engineering, University of Leeds, Leeds, UK*

²*National Institute of Informatics, 2-1-2 Hitotsubashi, Chiyoda, Tokyo 101-0003, Japan.*

³*NTT Basic Research Laboratories, NTT Corporation,*

3-1 Morinosato-Wakamiya, Atsugi, Kanagawa, 243-0198, Japan.

Memory-assisted measurement-device-independent quantum key distribution (MA-MDI-QKD) is a promising scheme that aims to improve the rate-versus-distance behavior of a QKD system by using the state-of-the-art devices. It can be seen as a bridge between current QKD links to quantum repeater based networks. While, similar to quantum repeaters, MA-MDI-QKD relies on quantum memory (QM) units, the requirements for such QMs are less demanding than that of probabilistic quantum repeaters. Here, we present a variant of MA-MDI-QKD structure that relies on only a single physical QM: a nitrogen-vacancy center embedded into a cavity where its electronic spin interacts with photons and its nuclear spin is used for storage. This enables us to propose a simple but efficient MA-MDI-QKD scheme resilient to memory errors and capable of beating, in terms of rate and reach, existing QKD demonstrations. We also show how we can extend this setup to a quantum repeater system, reaching, thus, larger distances.

I. INTRODUCTION

Quantum repeaters (QRs) offer a fundamental solution to long-distance quantum key distribution (QKD) [1–4]. The main building blocks needed for the first generations of QRs are quantum memories (QMs). However, with the current technology, the requirements on QMs are too demanding to allow high-rate key exchange at long distances [5, 6]. Memory-assisted measurement-device-independent QKD (MA-MDI-QKD) is possibly the first step toward that end that can relax some of the constraints on the QMs and, at the same time, allows to enhance the rate-versus-distance behavior of a QKD system over a certain distance range [7, 8]. It resembles a single-node quantum repeater with QMs only in the middle site. The performance of such a system depends considerably on the QMs in use. Among the variety of QMs that can be used, nitrogen vacancy (NV) centers in diamond embedded into cavities are promising candidates for a real implementation of an MA-MDI-QKD setup [9–11]. In [9], the authors show that, by using the electron spin states of two NV centers, such a setup can outperform the conventional no-memory systems, as well as some other memory-assisted setups, in a moderate-to-high coupling regime. Here, we propose a new configuration that only uses one NV center. It relies on the nuclear spin of the NV center for storing quantum states, while using its electron spin to interact with light. The simplicity of our scheme, combined with its superb noise resilience, makes our setup suitable for implementation using a technology reachable in the near future.

The performance of an MA-MDI-QKD setup depends strongly on how fast the QMs in use can interact with light. MA-MDI-QKD can lead to practical advantages when, compared to a no-memory system, the repetition rate is not too slow. That would typically require a repetition rate on the order of tens-to-hundreds of MHz. This condition is met by certain types of QMs, whose interaction times can be on the order of nanoseconds. NV

centers, for instance, have an interaction time around 20 ns, which makes them a possible candidate for MA-MDI-QKD.

In addition, there must be some heralding mechanism that announces that the user’s state has been stored into the QM. One way of doing this is to teleport the user’s state into the QM through a side Bell-state measurement (BSM). In particular, the state sent by each user will interact with a photon previously entangled with certain internal degrees of freedom of the NV center. Hence, upon a successful BSM, the user’s state will be teleported into the QM. The success of the BSM on photons is heralded by a specific click pattern of the photodetectors used in the BSM module.

When such a heralding method is used, the rate will be limited by the time needed to entangle the photon with the QM. Therefore, the entangling process is fundamental to determining the fastest repetition rate that can be reached by such an MA-MDI-QKD setup. There are several ways to entangle a photon with a QM depending on the type of memories in use. The approach proposed in [9] relies on using two NV centers in diamond, one for each user, as QM units. In order to increase the probability of creating photon-QM entanglement, the NV centers are also embedded into a one-sided microcavity. With this cavity configuration, as well as with the assumption of a moderate coupling regime, the authors present a setup that allows to teleport the user’s state into the electron spin of the NV center through the so called double-encoding technique [9, 12]. For such a system, in [9], the authors calculate the secret key rate and compare it with that of other single-excitation QMs, such as quantum dots, trapped ions and trapped atoms. They show that NV centers embedded into microcavities outperform these other QMs.

The results in [9], while promising, may suffer from the limited coherence time of the electron spin of the NV center [13, 14], which makes the key rate of this system to drop to zero at a distance around 500 km [9]. Once

other non-idealities, such as the additional background noise from frequency converters [15], are accounted for, the window over which the NV-based system outperforms the no-memory one would even become narrower. It is therefore important to come up with a system that has a wide window of opportunity, so that in practice part of it can be exploited. For an NV center, such an enhanced performance can be achieved by using the nuclear spin whose coherence time is known to be much longer than that of the electron spin [16].

Motivated by the possibility of using the nuclear spin of an NV center as a storage unit, in this paper, we propose a new MA-MDI-QKD setup that relies on *only one* NV center as physical memory. In our setup, the electron spin is still being used to interact with photonic systems. Here, we first load the NV center electron spin with Alice's photon. Once a successful loading event takes place, the electron spin state is transferred to the nuclear one. We then proceed with loading the electron spin with Bob's photon. When the electron spin is loaded for the second time, specific operations on the electron and the nuclear spins will be performed to replicate a *deterministic* full BSM operation creating, thus, a correlated bit between the users.

For our proposed protocol, we calculate the secret key generation rate, as the main figure of merit, and compare it with the fundamental bound, as obtained in Ref. [17] and referred to by PLOB, hereafter, on the key rate of repeaterless QKD systems. Our analysis accounts for major sources of imperfection such as the decoherence and gate errors in the QM as well as dark current in detectors and path loss. Moreover, we will show how this scheme can be extended to a quantum repeater setup, for which we estimate the longest secure distance possible.

The paper is structured as follows. In Sec. II we present our single-memory MA-MDI-QKD scheme. In Sec. III, we describe our methodology for calculating the secret key generation rate for the proposed protocol. We continue by providing some numerical results in Sec. IV, before drawing our conclusions in Sec. V.

II. SINGLE-MEMORY MDI-QKD

Our single-memory MDI-QKD scheme belongs to the set of MA schemes that use indirect heralding; see Fig. 1(a). This set allows faster writing times as compared to certain directly heralding memories [8]. In Fig. 1(a), we first entangle a photon with some internal degrees of freedom of the QM, and then interfere this photon and the one sent by the user at a side-BSM. If the side-BSM is successful, the user's state has ideally been teleported into the QM. In [9], this required entangling operation is done by the double-encoding module in Fig. 2. This module relies on a cavity-based NV center that, depending on its internal state, would impose a different phase shift on an impinging single photon. As a result, an entangled photon with the electron spin of the NV center

can ideally be obtained. We have summarized the details of this procedure in Appendix A.

Our proposed scheme in Fig. 1(b) relies on the same double-encoding scheme as in Fig. 2, but it differs from the scheme in Fig. 1(a) in several ways. First, we have replaced the two physical QMs in Fig. 1(a) with only one NV center in Fig. 1(b). In Fig. 1(b), both users send BB84 encoded photons at a similar repetition period, T , to the middle site, at which, with the same period, a photon is double encoded with the NV center electron spin. At this site, we first switch the photons sent from, for instance, the left user (Alice) to the BSM module in Fig. 1(b) until a successful loading occurs. That is, the state of Alice is teleported to the electron spin. At this point, we transfer the electron spin state to the nuclear one, and, in the meantime, rearrange the switch to now direct the photons sent from the user on the right (Bob) to the BSM module. The required optical switch here just needs to act like a rotating mirror, and can be implemented using fast switching technologies [18]. Once we get the second successful loading event, the NV center contains the state of Alice in its nuclear spin and that of Bob in its electron spin. We just then need a BSM operation on these two systems to share a key bit between Alice and Bob. The final BSM can be done deterministically, although with some possible errors [19], which we account for in our key rate analysis. The detailed description of the above steps is given in Appendix B.

An interesting feature of our proposed scheme is that by adding another NV center to the scheme of Fig. 1(b) we can implement a three-leg quantum repeater setup, as shown in Fig. 1(c), with equidistant segments. This repeater system works in two phases. First, we entangle the electron spins of the two NV centers in Fig. 1(c), which are separated by a distance $L_0 = L/3$. This can be done by double encoding a photon with each QM and then performing a BSM on the two photons. Considering NV centers embedded in cavities, this procedure is expected to succeed with a probability proportional to the channel transmissivity. We then transfer the entangled state of the electron spins to the nuclear spins and that will complete phase 1 of the protocol. In phase 2, we continue double encoding photons with the electron spins, but now direct these photons to the side BSM modules in Fig. 1(c) using optical switches. As soon as a successful side-BSM occurs, we can proceed to perform a deterministic BSM on the nuclear and electron spin of that QM as before. Note that, throughout both phases, users are sending their encoded photons to the side BSM, but the middle sites do not activate the side BSM modules until entanglement between the two QMs is established. When both middle sites have swapped entanglement, we are left with a shared key bit between the two end users. Note that a similar but extended version of our three-leg quantum repeater has been proposed in [10]. They, however, use the double-heralding technique for the initial entanglement [20], which is suitable for NV centers without a cavity, but its rate scales with the product of the chan-

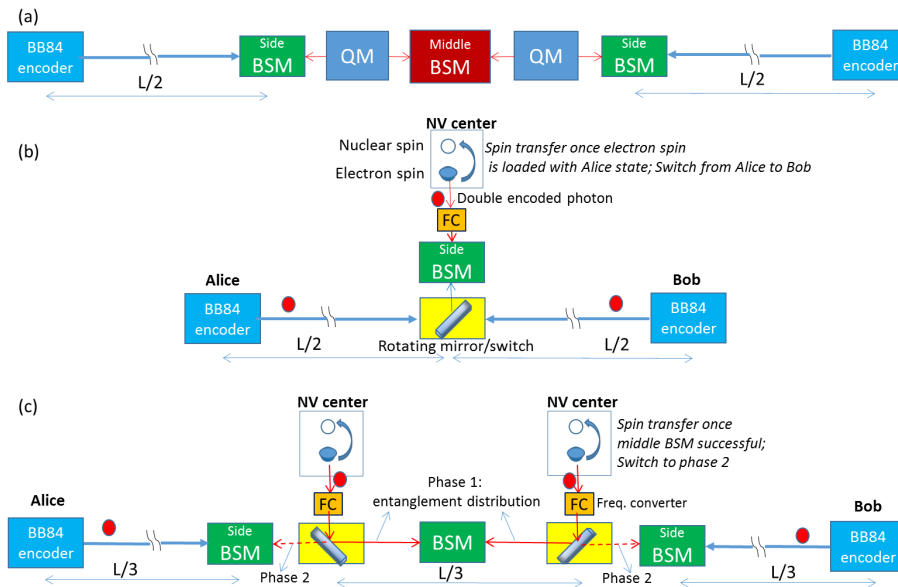


Figure 1. MA-MDI-QKD with (a) two non-heralding physical memories, (b) a single memory with two qubits, and (c) its extension to a three-leg quantum repeater system.

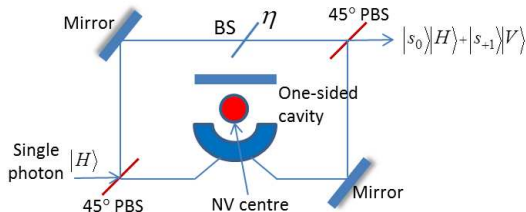


Figure 2. The double-encoding module proposed in [9]. It allows to entangle a polarized photon with an NV center in a cavity. This module will be used for transferring users' states into the electron spin of the NV center.

nel transmissivity and the NV center coupling efficiency. The latter is a limiting factor when cavity enhancement is not present and would reduce the achievable rate in the system.

III. KEY RATE ANALYSIS

In this section the secret key generation rate of the proposed setup of Fig. 1(b) is obtained under the normal operation conditions when no eavesdropper is present. We will also estimate the key rate of the quantum repeater scheme of Fig. 1(c). We assume that Alice and Bob use single photons in their encoders. This is not a fundamental restriction but it provides a convenient approach to compare memory-assisted schemes with the no-memory MDI-QKD systems. It is also possible to use decoy states, for which similar margins of improvement over decoy-state no-QM systems are expected. In [8], the

total secret key generation rate, using the efficient QKD protocol when ideal single photon sources are used by the users and the Z basis is more often used than the X basis, is lower bounded by the following expression

$$R_{\text{QM}} = \frac{R_S}{N_L(P_A, P_B) + N_r} Y_{11}^{\text{QM}} (1 - h(e_{11;X}^{\text{QM}}) - fh(e_{11;Z}^{\text{QM}})), \quad (1)$$

where P_A and P_B are the probability of a successful side-BSM on, respectively, Alice and Bob's side; Y_{11}^{QM} is the probability that the middle BSM is successful assuming that both memories are loaded (in the Z basis); $e_{11;X}^{\text{QM}}$ and $e_{11;Z}^{\text{QM}}$ are, respectively, the quantum bit error rate (QBER) between Alice and Bob in the X and Z basis when single photons are sent by the users; f is the inefficiency of error correction; $h(q) = -q \log_2 q - (1 - q) \log_2 (1 - q)$ is the binary entropy function; $R_S = 1/T$ is the repetition rate; N_L is the average number of trials to load both memories, which is given by $1/P_A + 1/P_B$; and, $N_r = \lceil \tau_r/T \rceil$ is the number of additional rounds needed for reading and initializing the QM, as well as any other required processing. The time corresponding to these tasks is denoted by τ_r .

In a real experiment, one needs to estimate the above parameters in order to use an appropriate level of error reconciliation and privacy amplification. Fortunately, in the limit of sufficiently long keys, all these parameters can be estimated accurately by conventional statistical techniques that correspond count rates to probabilities. If we use ideal single-photon sources, as we assume here, Y_{11}^{QM} , $e_{11;X}^{\text{QM}}$, and $e_{11;Z}^{\text{QM}}$ can directly be estimated from the observed measurements. In the case of decoy-state encoding, we can use known techniques for bounding these parameters even in the finite-size key setting [21–23]. Al-

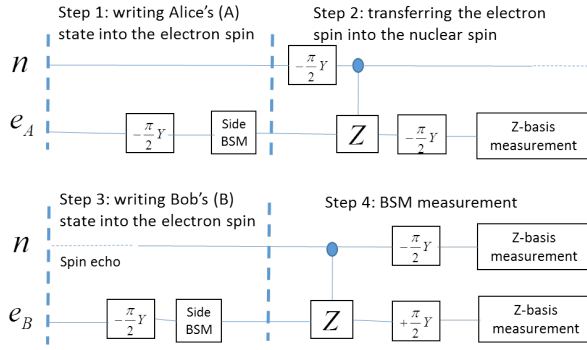


Figure 3. Schematic diagram for the sequential operations in the protocol on each of the nuclear (n) and electron (e) spins. The subscript A (B) refers to the interaction of the electron spin with Alice (Bob) photon. The detailed description of each step and its required operations is given in Appendix B.

though we do not account for finite-size key effects in this comparative analysis, it is expected that MA-MDI-QKD, because of its better loss tolerance, would be less affected by this issue than its no-QM counterparts.

A. Timing of the protocol

Figure 3 schematically shows different steps of our protocol and what operations each of the electronic and nuclear spins would go through. In step 1, we try to load Alice's photon. For each photon, we need to initialize the QM, which takes τ_{init} , entangle a photon with it, taking τ_{int} , and then do the side-BSM, taking τ_M . Once we get to Bob's photon (step 3), in addition to these operations, we also use spin echo, with a time parameter τ_{dis} , to disentangle the electron from the nuclear spin and to minimize any back action on the stored state in the nuclear spin. The fastest we can repeat the protocol then is given by $T = \tau_{\text{init}} + \tau_{\text{int}} + \tau_{\text{dis}} + \tau_M = \tau_w$. In principle, this can be done faster for Alice's photon at $T = \tau_w - \tau_{\text{dis}}$, but we ignore this possible advantage in our analysis.

In addition to capturing Alice and Bob's photons, in Fig. 3, we also need to transfer the state of electron spin to the nuclear spin (step 2), taking a time denoted by τ_{swap} , and finally do a deterministic BSM on the two spins (step 4) taking τ_{BSM} . In which case, $\tau_r = \tau_{\text{swap}} + \tau_{\text{BSM}} + \tau_{\text{init}}$.

B. Error Analysis

In order to calculate the elements of Eq. (1), in our simulation, we use the same approach as the one used in [9] with regard to the modeling of the decoherence, loss, dark count and detection efficiency. In addition to those errors, here, we particularly account for the errors in each of the logic gates of Fig. 3 by using a depolarizing channel inspired model. In particular, for a single-qubit

logic gate R_k on spin $k = e, n$, we assume that the joint state of electron-nuclear spins ρ_{en} undergoes the following transition:

$$\rho_{en} \rightarrow (1 - p_k) R_k \rho_{en} R_k^T + \frac{p_k}{3} (X_k \rho_{en} X_k + Y_k \rho_{en} Y_k + Z_k \rho_{en} Z_k), \quad (2)$$

where X_k , Y_k , and Z_k are the Pauli matrices of spin k and p_k is the corresponding depolarization parameter.

The only two-qubit gate in Fig. 3 is the controlled-Z (CZ) gate, whose operation is modeled as follows:

$$\rho_{en} \rightarrow (1 - p_{\text{CZ}}) O_{\text{CZ}} \rho_{en} O_{\text{CZ}} + p_{\text{CZ}}/3 (X_e X_n \rho_{en} X_e X_n) + p_{\text{CZ}}/3 (Y_e Y_n \rho_{en} Y_e Y_n) + p_{\text{CZ}}/3 (Z_e Z_n \rho_{en} Z_e Z_n), \quad (3)$$

where O_{CZ} represents the ideal CZ gate operation. In principle, one can also include additional error terms for different electron-nuclear Pauli operators. But, numerically, we find the above model sufficiently accurate for the purposes pursued in this paper.

Using the above models, we can obtain the state of the system at any step in Fig. 3. The derivations are cumbersome and have mostly been done by the software Maple. In short, for each scheme, we first obtain the state of the QMs once the user's state is loaded to them. At this stage, we also find P_A and P_B by including the number of rounds lost due to the deadtime as explained in [9]. Finally, we calculate the remaining terms in Eq. (1), i.e., Y_{11}^{QM} , $e_{11;X}^{\text{QM}}$, and $e_{11;Z}^{\text{QM}}$.

C. Three-leg Repeater

In principle, we can use the above detailed analysis to calculate the rate for the repeater setup in Fig. 1(c). But, as will be shown later, our scheme is quite resilient to existing gate errors. We therefore only provide a rough estimate of the key rate for the repeater scheme of Fig. 1(c). To that end, we calculate the average time T_{rep} that it takes to generate a raw key bit between Alice and Bob. This parameter includes the average time T_{ent} that it takes to entangle the two electron spins, the time to transfer the electron spins to nuclear spins, perform BSM operations on the two, and initialize the QMs again, whose sum we denoted earlier by τ_r , as well as the time T_{load} for loading electron spins with Alice and Bob photons. In this case, we have

$$T_{\text{rep}} = T_{\text{ent}} + \tau_r + T_{\text{load}}, \quad (4)$$

where

$$T_{\text{ent}} \approx T_0 / P_{\text{ent}} \quad (5)$$

with $T_0 = (L/3)/c$ being the transmission delay in the middle link (with c being the speed of light) and

$$P_{\text{ent}} = (1/2)(\eta_{\text{ms}}\eta_{\text{nc}}\eta_{\text{nd}})^2 e^{-(L/3)/L_{\text{att}}} \quad (6)$$

Entangling efficiency, η	0.9
Cooperativity, C	50
Single photon source efficiency, η_s	0.72
Frequency conversion efficiency, η_c	0.68
Detector efficiency, η_d	0.93
Dark count rate [24]	1 cps
Attenuation length, L_{att}	25 km
Speed of light in fiber, c	2×10^8 m/s
Initialization time, τ_{init}	11.5 ns
Interaction time, τ_{int}	10 ns
Verification time, τ_M	1 ns
Swap time, τ_{swap}	1.1 μs
Deterministic BSM time, τ_{BSM}	1.5 μs
Error probability of the $\pm \frac{\pi}{2} Y$ gate for the electron spin, p_e	10^{-3}
Error probability of the CZ gate, p_{CZ}	2×10^{-4}
Error probability of the $-\frac{\pi}{2} Y$ gate for the nuclear spin, p_n	10^{-3}

Table I. Nominal values used in our numerical results.

being the success probability of a polarization-based entanglement distribution scheme where photons are entangled with QMs and a probabilistic BSM will be performed on these photons in the middle of the link. Here, η is the efficiency of the double encoding module of Fig. 2, η_s is the efficiency of the single-photon source used in that module, η_d is the detector efficiency, η_c is the frequency converter efficiency, and L_{att} is the attenuation length of the channel. In Eq. (6), $\eta\eta_s\eta_c$ represents the probability of entangling a photon with the electron spin, $\eta_d^2/2$ represents the BSM success probability, and $\exp(-L/3/L_{\text{att}})$ represents the channel loss. Finally, in Eq. (4),

$$T_{\text{load}} \approx (3/2)T/P_A, \quad (7)$$

which accounts for the average time needed to load both photons assuming that $P_A = P_B$ [8]. Using the above timing calculations, we then estimate the secret key rate of the setup of Fig. 1(c) by $R_{\text{rep}} = 1/T_{\text{rep}}$. Note that this is an optimistic estimate of the rate in which memory errors are not accounted for.

IV. NUMERICAL RESULTS

In this section, we compare the rate of our proposed single-memory MDI-QKD scheme with the PLOB bound of a repeaterless QKD system reported in Ref. [17]. For a pure-loss channel with a total transmissivity η_T , the maximum achievable secret key rate per transmitted pulse in a repeaterless system is given by $\log_2(1 - \eta_T)$. In our simulations, we assume that $\eta_T = \exp(-L/L_{\text{att}})\eta_d$. We multiply this bound by relevant clock rates in no-QM systems to obtain a bound on the total key rate. We also estimate the rate of the three-leg quantum repeater

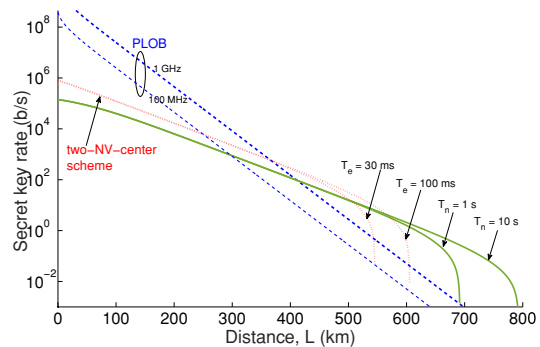


Figure 4. Secret key generation rates versus distance for our proposed single-memory MDI-QKD scheme and its comparison with a no-QM system (PLOB) driven at 100 MHz (lower curve) and 1 GHz (upper curve) as well as the two-QM setup proposed in [9]. In the latter case, the coherence time of the electron spin, T_e , ranges from 30 ms to 100 ms. T_n refers to the coherence time of the nuclear spin, which is the relevant time constant for the setup proposed here.

scheme that relies on our proposed scheme of Fig. 3(c). The nominal values used in our numerical analysis are summarized in Table I. These values are taken from the state-of-the-art technologies for various quantum devices. The time and error parameters of the NV centers is taken from the rigorous analysis in [25]. In our analysis, we also consider the use of frequency converters to allow the interaction between a QM-driven photon and the telecom photon sent by the user. We model this as an additional source of loss, which modifies the efficiency of the side-BSM detectors [26, 27].

A. Single-memory MDI-QKD

Figure 4 compares the secret key generation rate of our proposed single-memory MDI-QKD scheme with two different alternatives: the PLOB bound and the two-QM scheme in [9]. The rate of our proposed scheme outperforms the PLOB bound at a distance around 400 km if we assume that the repeaterless system is driven by an ideal single-photon source with a pulse rate of 1 GHz. In Fig. 4, we have also included a PLOB curve when the pulse rate of the ideal source is 100 MHz. This somehow replicates the practical case where, instead of single-photon sources, one may use the decoy-state technique. For decoy-state encoding, when the average number of photons per signal state is 0.5, only 30% of the time we generate single-photon states. If one accounts for the percentage of the time that the signal state, rather than decoy states, may be used, one can argue that only about 10%-20% of the pulses sent will carry single-photon states. That is even if we send 1 Gpulse/s, only 100-200 Mpulse/s would carry single-photon information. The lower PLOB curve in Fig. 4 shows this scenario by calculating the rate for an ideal single-photon source with a pulse rate of 100 MHz.

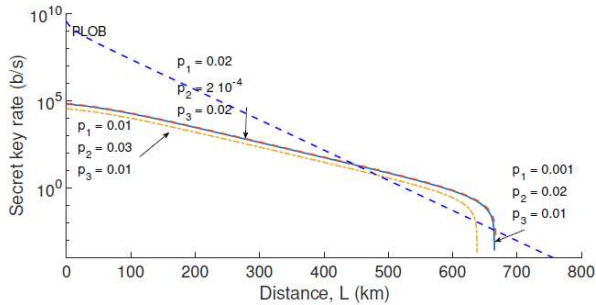


Figure 5. Secret key generation rates versus distance for our proposed single-memory MDI-QKD scheme and its comparison with no-QM MDI-QKD driven at 1 GHz for different values of error probabilities associated with the logic gates of Fig. 3.

In this case, the cross-over distance is around 300 km.

Our scheme offers a slightly lower rate than that of the two-NV-center scheme in Ref. [9] at short-to-medium distances, but can extend the maximum security distance by a few hundred kilometers. The reason for the drop in rate is partly due slower repetition rates. In our scheme, we consider doing spin echo in every round, which takes around $\tau_{\text{dis}} = 20$ ns, and that would almost reduce the repetition rate by a factor of two. We instead do the middle BSM deterministically, which should buy us a factor of two if we had no errors in our operations. But, then, instead of loading both memories in parallel as in [9], we do it sequentially, and that is why the starting rate for the scheme of Ref. [9] is a bit higher. As we get to longer and longer distances, the decoherence issue with electron spin states, in the scheme of Ref. [9], would kick in, whereas our single-QM scheme, which relies on nuclear spins, is still resilient to decoherence errors. As a result, the maximum security distance considerably improves, and that gives us some more immunity against other sources of noise that may exist in a realistic setup. Moreover, in terms of resources, the scheme of Fig. 1(b) uses almost half of major devices needed in the scheme of Ref. [9]. If we consider the normalized rate per resources used, as a figure of merit, then the two schemes offer similar rates, but the one that uses nuclear spins cover longer distances.

Another source of error that may limit the performance of our system is the errors associated with the logic gate operations of Fig. 3. In [25], the authors analytically estimate the errors caused by these operations for different values of the pump strength. However, in a real experimental setup they could differ from the results obtained in [25]. Therefore, we also estimate the highest error tolerable by our system within which it is still possible to have an improvement over the PLOB bound. Figure 5 shows several extreme cases where p_e , p_n , and p_{CZ} take rather large values on the order of 0.01. It can be seen that, at $T_n = 1$ s, even such high error terms will kick in after 600 km of channel length. Note that the tolerable error rate is over one order of magnitude higher

than the expected nominal values. That would give us assurance that such a setup, once extended to a quantum repeater setting, can tolerate multiple rounds of entanglement swapping without any need for purification.

In addition to gate errors and memory decoherence, there are other practical aspects that one needs to deal with in a realistic scenario. For instance, the single-photon source used in the middle of the link must have very low two-photon emission rates otherwise, these additional photons may cause errors in the system [28]. In our case, the middle QMs are driven by NV-center-based single-photon sources that have a very similar structure to the QMs themselves. The chance of multiple-photon emission is then naturally kept low. Note that the multiple photon terms generated by the users, in a decoy-state scenario, would not cause much problems as they go through a lossy channel. Similarly, one should be aware of the background noise generated by external sources, such as classical channels propagating over the same fiber medium as the quantum ones [29], or by the frequency converters. By proper design and filtering [30], this should be achievable in practice. Our scheme also additionally needs a 2×2 optical switch to swap between two users. For such a switch one should consider the insertion loss as well as the switching time. The latter issue is less of a problem in our case, as, in the limit of long distances, the time between two consecutive photons surviving the path loss is rather long, and that would alleviate the requirements on the switching time. In such a case, for such a small-size switch, the insertion loss could also be sufficiently low. In our numerical results, we have neglected the switching insertion loss. Finally, in practice, it is rarely the case that the distance between the user nodes and the middle node are identical. While this may cause us to deviate from the optimal performance, the effect can easily be modeled within our framework. The result is not expected to be much different from that of an asymmetric no-QM MDI-QKD setup.

B. Three-leg Repeater

Now that we establish that the errors arising from our logic gates is very low, we can reliably use the estimate in Sec. III C to calculate the key rate of the quantum repeater setup of Fig. 1(c). For simplicity, we have also ignored the effect of dark count. For a dark count rate of 1 cps, and assuming pulse widths on the order of nanoseconds, the dark count will become important when $L/3$ is comparable to 450 km. We should therefore be able to cover distances up to around 1400 km using this simple repeater setup. If other sources of background, such as the Raman noise from classical channels or the frequency converters, kick in, then the corresponding maximum length would be reduced.

Figure 6 shows the comparison between the single-memory MDI-QKD scheme at $T_n = 1$ s and its quantum repeater extension of Fig. 1(c). It can be seen that

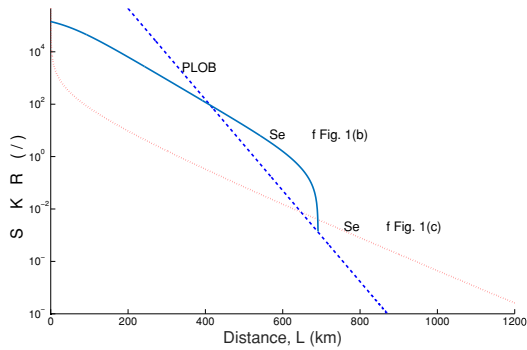


Figure 6. Secret key generation rates versus distance for the quantum repeater setup of Fig. 1(c) and our proposed single-memory MDI-QKD scheme at $T_n = 1$ s.

the repeater setup outperforms the PLOB bound around 600 km, where the rate is already very low at around $R_{\text{rep}} \sim 10^{-2}$ /b/s). In order to increase the rate, we might consider a multiple memory configuration as proposed in [5, 31–33] or use more nesting levels as in Ref. [10]. In [10], the authors calculate the secret key rate versus the distance for different values of the gate efficiency with and without entanglement distillation. In order to reach long distances, they however need gate efficiencies around 0.99. Such high efficiencies may be possible if one uses the cavity setting that we have assumed for the NV centers. In any case, the general repeater setup still seems to be very hard to implement with current technologies.

V. CONCLUSIONS

In this paper, we presented a new MA-MDI-QKD system, which relied on only one physical memory: an NV center embedded in a small-volume optical cavity. We calculated the secret key rate for such a system and we compared it with the fundamental bound for a repeaterless QKD system as well as with the two-NV-center system proposed in [9]. In our new system, for storage, we relied on the nuclear spin of the NV center, which could have a coherence time as long as 10 seconds. For such a value of coherence time, we showed that the rate of our system can reach longer distances compared to the scheme proposed in [9], while the normalized rate per NV center module used was about the same. We also determined the highest tolerable error probability for each logic gate operation required to extract a secret key when we use this scheme. We compared these threshold error rates with what is expected from these devices, and showed that we had sufficient room to accept additional error in the system.

While MA-MDI-QKD is a good approach to enhance the rate-versus-distance behavior of a QKD system, in order to achieve longer distances, we need a quantum repeater setup. Therefore, we showed how we could extend our single-memory system to a simple quantum re-

peater setup by adding one more memory and splitting the channel into three equidistant elementary links. For such a setup, we estimated the longest distance achievable by considering the time intervals required for each single operation. We showed that we could reach a total distance of about 1400 km. After this distance the dark count rate would become dominant not allowing to extract a secret key. Despite the longer distance the quantum repeater setup allowed us to reach, its rate was very low. To address such an issue, we should consider a multiple memory configuration. In this way we can speed up the probability of storing the users' states into the memories. Nevertheless, the single-memory scheme presented in this paper offered a simple implementation, which could be extended to a quantum repeater system in the future.

ACKNOWLEDGMENTS

This work was partly funded by the UK's EPSRC Grant EP/M013472/1 and EPSRC Grant EP/M506951/1, and the EU's H2020 programme under the Marie Skłodowska-Curie project QCALL (GA 675662).

Appendix A: Double encoding scheme

In this Appendix, we review the entangling scheme used in [9], shown in Fig. 2, known as the double-encoding module. The double-encoding scheme is used to entangle a photon with the electron spin states of the NV center. To this end, the NV center is embedded into a one-sided cavity, whose effective reflectivity is affected by the internal state of the NV center. The idea of conditional reflectivity has already been proposed in [34] for a trapped atom system. In particular, in [9], the authors show that when the NV center is in the electron spin state 0, $|s_0\rangle$, then the incoming photon to the module of Fig. 2 will be reflected off the cavity. When the NV center is in the electron spin state +1, $|s_{+1}\rangle$, then the photon will also be reflected but it will acquire a π phase. This implies that in both cases the photon will be reflected but with a different phase shift.

The module of Fig. 2 ideally works as follows. First the NV center is initialized into the state $|\Psi_{in}\rangle = (|s_0\rangle + |s_{+1}\rangle)/\sqrt{2}$. Then, we generate an H -polarized single photon and send it through a $+45^\circ$ polarizing beam splitter (PBS). We can generate such a single photon by driving a specific transition in another cavity-NV-center pair [9]. In Fig. 2, the $+45^\circ$ -polarized component of this single photon interacts with the NV center, resulting in the joint state $|D\rangle_s (|s_0\rangle - |s_{+1}\rangle)/\sqrt{2}$, where $|D\rangle = \frac{1}{\sqrt{2}}(|H\rangle + |V\rangle)$. The photonic modes r and s are then recombined at a second $+45^\circ$ PBS, which will

result in the following output state

$$|\Psi_2\rangle = \frac{1}{\sqrt{2}}(|H\rangle|s_0\rangle + |V\rangle|s_{+1}\rangle). \quad (\text{A1})$$

In deriving Eq. (A1), we have made the assumption that the reflection coefficients, in the two cases of $|s_0\rangle$ and $|s_{+1}\rangle$ states, has the same magnitude of 1. However, for finite values of the cooperativity C the two coefficients may have different values, leading to a deviation from the ideal entangled state in Eq. (A1). As a consequence, this will cause an imbalance between the two legs of the interferometer in Fig. 2. We can fix this by adding a beam splitter with transmissivity η in the r branch. The value of η will be chosen accordingly to account for different sources of loss in the s branch. In this case, the generated state by our double-encoder will become [9]

$$\rho_{\text{NV-P}} = \eta|\Psi_2\rangle\langle\Psi_2| + (1-\eta)|\mathbf{0}\rangle_{\text{PP}}\langle\mathbf{0}| \otimes I'_{\text{NV}}, \quad (\text{A2})$$

where $I'_{\text{NV}} = (|s_0\rangle\langle s_0| + |s_{+1}\rangle\langle s_{+1}|)/2$.

The output state of Eq. (A2) will teleport the state sent by the user into the QM in most of the cases when the side-BSM is successful. The vacuum term will introduce a small error that is proportional to the dark count. However, this error will not be relevant as we will show in our calculation of the secret key rate.

Another practical assumption is considering a strong coupling regime for the NV center embedded into the cavity. To this aim we consider a cooperativity $C = 50$. In [9], the authors show that for lower values of C , the reflection coefficients of the cavity strongly depend on the state of the NV center. On one hand, as C decreases, when the NV center state is $|s_0\rangle$ the reflection coefficient decreases as well and, on the other hand, when the NV center state is $|s_{+1}\rangle$ the reflection coefficient approaches 1. In this case, as C decreases, the key rate decreases as well. However, it is still possible to extract a secret key for a value of C as low as 1.22 [9]. For the sake of simplicity, in our calculation, we assume that the NV center is in the strong coupling regime so we can use Eq. A2 as output density matrix describing the double-encoded state of the polarized photon with the NV center.

At the beginning of each round, before performing the double encoding operation discussed above, we have to initialize the NV center in state $|\Psi_{in}\rangle$. The initialization process can be performed using the double-encoding module of Fig. 2. In every round, we send an H -polarized single photon to the NV-center-cavity module, and measure the polarization of the output photon in $|H\rangle$ and $|V\rangle$ basis. Depending on which photodetector will click, we could infer the corresponding state of the NV center, i.e. $|s_0\rangle$ or $|s_{+1}\rangle$. Then we apply the relevant rotation to initialize the NV center in $|\Psi_{in}\rangle$. The above procedure includes the double encoding operation and a rotation. The time for the double-encoding operation is given by the time needed for the photon to interact with the NV center, τ_{int} , i.e. the interaction time, which takes roughly 10 ns. The rotations on the electron spin can be driven

by using a microwave driving field perpendicular to the NV center axis without the same drive also affecting the nuclear spin [25]. In [25], the authors analytically calculated the timing and the error associated to the rotations required to initialize the NV center. They depend on the pump strength of the driving field [25]. In our work, we assume that the pump strength is 375 MHz, which will rotate the electron spin in roughly 1.5 ns. Therefore, adding up both these operations we get 11.5 ns, which corresponds to the initialization time, τ_{init} , in our protocol.

In the above procedure, if we get no click, then we consider that the initialization process has failed. This can happen for several consecutive rounds, which indicates that the memory is in a deadtime period [9]. During this period, the NV center is in certain metastable states, which will decay to any of $|s_0\rangle$ and $|s_{\pm 1}\rangle$ states [9]. Since $|s_{-1}\rangle$ does not correspond to any desired state, during the deadtime, we swap states $|s_0\rangle$ and $|s_{-1}\rangle$ in every initialization round to avoid the possibility that the NV center stays in the state $|s_{-1}\rangle$ for ever.

Appendix B: Single-memory MDI-QKD protocol

Figure 3 shows the steps containing all the required logic gates that must be applied to the electron and nuclear spin of the NV center in order to extract a secret key in the scheme of Fig. 1(b). The upper line in each section of Fig. 3 refers to the gate operations applied to the nuclear (n) spin and the lower line refers to the gate operations applied to the electron (e_A , e_B) spin of the NV center. The subscripts A and B of the electron spin refer to the event of storage of the electron spin with Alice's and Bob's state, respectively.

The single-memory MDI-QKD protocol works as follows, see Fig. 3.

Step 1, Alice Teleportation: The first step consists of a $-\frac{\pi}{4}$ rotation around the Y axis of the electron spin of the NV center, which will initialize the electron spin into the state $|\Psi_{in}\rangle$, and a side-BSM, which, if successful, will project the user's state into the electron spin. These two operations are represented by the $-\frac{\pi}{2}Y$ gate and Side-BSM in Fig. 3. Rotations on the electron spin can be implemented by using a microwave driving field perpendicular to the NV center as explained in [25].

Step 2, Spin Transfer: Once the electron spin has been written with the user's state, we perform a $-\frac{\pi}{2}Y$ rotation on the nuclear spin, which will create the state $|n_+\rangle = \frac{1}{\sqrt{2}}(|\uparrow\rangle + |\downarrow\rangle)$, where $|\uparrow\rangle$ and $|\downarrow\rangle$ are, respectively, the up and down nuclear spin states in the Z -basis. After that, we let the nuclear spin interact with the electron spin through the always-on hyperfine interaction with Hamiltonian $H_{\text{eff}} = \hbar A_{\text{net}}|s_1\rangle\langle s_1| \otimes |\uparrow\rangle\langle\uparrow|$, where A_{net} is the coupling strength as explained in the supplementary material of Ref. [16]. The hyperfine interaction provides a route to entangling the spins without resorting to driving fields or varying the magnetic fields

dynamically [25]. In fact, if we assume that the electron spin is in state $|\Psi_e\rangle = \alpha|s_0\rangle + \beta|s_1\rangle$, where α and β are arbitrary coefficients corresponding to the state sent by the user, the joint state of the nuclear-electron system after the nuclear-spin rotation will be given by

$$|\psi\rangle_{ne} = |n_+\rangle|\Psi_e\rangle. \quad (\text{B1})$$

If we now let this state evolve according to H_{eff} , we obtain

$$|\psi\rangle_{ne} = \alpha|s_0\rangle|n_+\rangle + \beta|s_1\rangle(|\downarrow\rangle + e^{iA_{\text{net}}t}|\uparrow\rangle)/\sqrt{2}. \quad (\text{B2})$$

At $t = \pi/A_{\text{net}}$, which roughly corresponds to $t = 165$ ns, the above state will become

$$|\psi\rangle_{ne} = \alpha|s_0\rangle|n_+\rangle + \beta|s_1\rangle|n_-\rangle, \quad (\text{B3})$$

which represents the CZ operation on the initial state in Eq. (B1) with the nuclear spin as the control qubit. Now, in order to transfer the electron spin into the nuclear spin, we first rotate the electron spin by another $-\frac{\pi}{2}Y$ operation obtaining

$$|\psi\rangle_{ne} = [\alpha(|s_0\rangle + |s_1\rangle)|n_+\rangle + \beta(|s_0\rangle - |s_1\rangle)|n_-\rangle]/\sqrt{2}. \quad (\text{B4})$$

If we now measure the electron spin by using the double-encoding procedure described in Appendix A, which corresponds to a Z-basis measurement gate in Fig. 3, the state of Eq. (B4) will become

$$|\psi\rangle_{ne} = \alpha|n_+\rangle \pm \beta|n_-\rangle, \quad (\text{B5})$$

where the sign depends on the outcome of the measurement.

The user's state is now stored into the nuclear spin. Note that the nuclear state undergoes a decoherence process, which has been taken into account in our calculation. However, in this case, we can rely on much longer coherence times as compared to the scheme of [9], due to the longer nuclear spin coherence time.

Step 3, Bob Teleportation: Now the other user, Bob, repeatedly tries to store his state into the electron spin with the same procedure as in step 1. The only difference is that we now have to do spin echo in every round to preserve the state of the nuclear spin and prevent a back action on the nuclear spin due to external interactions with the electron spin.

Step 4, Final BSM: Finally, in step 4, we perform a CZ gate and an X-basis measurement on both electron and nuclear spins as shown in Fig. 3. As explained in step 2, the X measurements are done by rotating the spins and then performing a Z measurement. This is equivalent to performing a full BSM in order to create a correlated bit between Alice and Bob. Depending on which basis and state Alice and Bob pick, we can have different possible output states right before the final Z-basis measurements, in step 4, on nuclear and electron spins. These states are summarized in Table II. Based on this table, in the Z-basis, Alice and Bob, only need to account for the result of measurement on the nuclear

		Z-basis		X-basis			
Alice	Bob	$ s_0\rangle$	$ s_{+1}\rangle$	Alice	Bob	$ s_0\rangle$	$ s_{+1}\rangle$
H	H	\uparrow	\uparrow	+	+	$ n_+\rangle$	\times
V	V	\uparrow	\uparrow	-	-	$ n_-\rangle$	\times
H	V	\downarrow	\downarrow	+	-	\times	$ n_+\rangle$
V	H	\downarrow	\downarrow	-	+	\times	$ n_-\rangle$

Table II. Possible states of the electron and nuclear spin of the protocol of Fig. 3 right before the measurement. Here $|n_{\pm}\rangle = \frac{1}{\sqrt{2}}(|\uparrow\rangle \pm |\downarrow\rangle)$ and the cross symbol \times stands for an impossible event in the ideal case.

spin. A spin up means that they have both got similar bits, and a spin down implies the other case. If they have both chosen the X basis, then the electron spin would be in $|s_0\rangle$ if Alice and Bob share the same bit, and in $|s_{+1}\rangle$ if they have complementary bits.

-
- [1] H.-J. Briegel, W. Dür, J. I. Cirac, and P. Zoller, *Phys. Rev. Lett.* **81**, 5932 (1998).
- [2] L.-M. Duan, M. D. Lukin, J. I. Cirac, and P. Zoller, *Nature* **414**, 413 (2001).
- [3] W. J. Munro, A. M. Stephens, S. J. Devitt, K. A. Harrison, and K. Nemoto, *Nature Photon.* **6**, 771 (2012).
- [4] W. J. Munro, K. Azuma, K. Tamaki, and K. Nemoto, *IEEE Journal of Selected Topics in Quantum Electronics* **21**, 78 (2015).
- [5] N. Lo Piparo and M. Razavi, *IEEE Journal of Selected Topics in Quantum Electronics* **21**, 6600508 (2015).
- [6] S. Muralidharan, L. Li, J. Kim, N. Lütkenhaus, M. D. Lukin, and L. Jiang, *Sci. Rep.* **6**, 20463 (2016).
- [7] S. Abruzzo, H. Kampermann, and D. Bruß, *Phys. Rev. A* **89**, 012301 (2014).
- [8] C. Panayi, M. Razavi, X. Ma, and N. Lütkenhaus, *New J. Phys.* **16**, 043005 (2013).
- [9] N. Lo Piparo, M. Razavi, and W. J. Munro, *Phys. Rev. A* **95**, 022338 (2017).
- [10] S. Vinay and P. Kok, *Phys. Rev. A* **95**, 052336 (2017).
- [11] F. Rozpedek, K. Goodenough, J. Ribeiro, N. Kalb, V. C. Vivoli, A. Reiserer, R. Hanson, S. Wehner, and D. Elkouss, "Realistic parameter regimes for a single sequential quantum repeater," arXiv:1705.00043 (2017).
- [12] D. E. Bruschi, T. M. Barlow, M. Razavi, and A. Beige, *Phys. Rev. A* **90**, 032306 (2014).
- [13] N. Bar-Gill, L. M. Pham, A. Jarmola, D. Budker, and R. L. Walsworth, *Nature Communications* **4**, 1743 (2013).
- [14] P. C. Maurer, G. Kucsko, C. Latta, L. Jiang, N. Y. Yao, M. Markham, D. J. Twitchen, J. I. Cirac, and M. D. Lukin, *Science* **336**, 1283 (2012).
- [15] N. Lo Piparo, N. Sinclair, and M. Razavi, "Memory-assisted quantum key distribution resilient against

- multiple-excitation effects," arXiv:1707.07814 (2017).
- [16] K. Nemoto, M. Trupke, S. J. Devitt, A. M. Stephens, B. Scharfenberger, K. Buczak, T. Nöbauer, M. S. Everitt, J. Schmiedmayer, and W. J. Munro, *Phys. Rev. X* **4**, 031022 (2014).
- [17] S. Pirandola, R. Laurenza, C. Ottaviani, and L. Banchi, *Nature Commun.* **8**, 15043 (2017).
- [18] A. Bogoni, X. Wu, S. R. Nuccio, J. Wang, Z. Bakhtiari, and A. E. Willner, *Selected Topics in Quantum Electronics*, *IEEE Journal of* **18**, 709 (2012).
- [19] N. Lo Piparo, M. Razavi, and W. J. Munro, in *Quantum Communications, Measurement, and Computing Conference* (2016).
- [20] H. Bernien, B. Hensen, W. Pfaff, G. Koolstra, M. S. Blok, L. Robledo, T. H. Taminiau, M. Markham, D. J. Twitchen, L. Childress, and R. Hanson, *Nature* **497**, 86 (2013).
- [21] X. Ma, C.-H. F. Fung, and M. Razavi, *Phys. Rev. A* **86**, 052305 (2012).
- [22] M. Curty, F. Xu, W. Cui, C. C. W. Lim, K. Tamaki, and H.-K. Lo, *Nature Communications* **5**, 3732 (2014).
- [23] Z. Zhang, Q. Zhao, M. Razavi, and X. Ma, *Phys. Rev. A* **95**, 012333 (2017).
- [24] F. Marsili, V. B. Verma, J. A. Stern, S. Harrington, A. E. Lita, T. Gerrits, I. Vayshenker, B. Baek, M. D. Shaw, R. P. Mirin, and S. W. Nam, *Nat. Photon.* **7**, 210 (2013).
- [25] M. S. Everitt, S. Devitt, W. J. Munro, and K. Nemoto, *Physical Review A* **89**, 052317 (2014).
- [26] R. Tang, X. Li, W. Wu, H. Pan, H. Zeng, and E. Wu, *Optics Express* **23**, 236046 (2015).
- [27] J. S. Pelc, L. Ma, C. Phillips, Q. Zhang, C. Langcrock, O. Slattery, X. Tang, and M. M. Fejer, *Optics Express* **19**, 21445 (2011).
- [28] N. Lo Piparo, M. Razavi, and C. Panayi, *IEEE Journal of Selected Topics in Quantum Electronics* **21**, 6601010 (2015).
- [29] S. Bahrani, M. Razavi, and J. A. Salehi, *Scientia Iranica D* **23**, 2898 (2016).
- [30] S. Bahrani, M. Razavi, and J. A. Salehi, in *Proc. SPIE*, Vol. 9900 (2016) pp. 99001C–99001C–7.
- [31] M. Razavi, M. Piani, and N. Lütkenhaus, *Phys. Rev. A* **80**, 032301 (2009).
- [32] J. Amirloo, M. Razavi, and A. H. Majedi, *Phys. Rev. A* **82**, 032304 (2010).
- [33] N. Lo Piparo and M. Razavi, *Phys. Rev. A* **88**, 012332 (2013).
- [34] L.-M. Duan and H. J. Kimble, *Physical Review Letters* **92**, 127902 (2004).